Title: Multiscale and Multiphysics FEA simulation and materials optimization for laser ultrasound transducers.

Authors: Sipan Liu^a, Howuk Kim^a, Wenbin Huang^b, Wei-Yi Chang^c, Xiaoning Jiang^{a*}, Jong Eun Ryu^{a*}

^a Department of Mechanical and Aerospace Engineering, North Carolina State University,
 1840 Entrepreneur Drive, Raleigh, NC 27695, USA

^b State Key Lab of Mechanical Transmission, Chongqing University, Chongqing, China ^c CTS Corporation, 4925 Indiana Ave, Lisle, IL 60532, USA

Abstract

The relationship between the nanocomposite design and the laser ultrasound transducer (LUT) characteristics was investigated through simulations in multiple scale levels for material behavior, device response, and acoustic wave propagation in media. First, the effects of the nanoparticle size and concentration on the effective properties of composites were quantitatively investigated with the finite element analysis (FEA) method. Second, the effective properties of the nanocomposite were assigned to the layer, which is modeled as a homogeneous material, in the FEA for the LUT simulating the energy conversion from the incident laser to the acoustic wave. Finally, the ultrasound propagation in the water was calculated by a theoretical wave propagation model. The FEA-based prediction was compared with the experimental data in the literature and a theoretical analysis for LUT based on Thermal-Acoustic coupling. As a result, the ultrasound waves on the transducer surface and at a distance in the water could be predicted. Based on the hierarchically integrated prediction procedure, the optimal conditions of the photoacoustic nanocomposites were investigated through the parametric study with the particle size and concentration as variables. The results guide the material designs optimized for different device characteristics, such as high pressure and broad bandwidth.

Keywords: Polymer-matrix composites (PMCs), Finite element analysis (FEA), Multiscale modeling, Acoustic emission, Laser ultrasound transducer

1 Introduction:

High amplitude and broadband acoustic pulses are usually preferred in terms of spatial resolution for ultrasound imaging and therapy [1–8]. However, developing ultrasound transducers with high intensity and broad bandwidth has been challenging. For example, the typical high intensity focused ultrasound (HIFU) piezo-based transducers usually have a high operation voltage requirement > 100 V [9], and some histotripsy HIFU need a higher voltage > 400V [10–13] to obtain the required negative pressure. For most piezo-based imaging transducers, the -6dB fractional bandwidth is below 80%, which can not meet the advanced imaging such as harmonic imaging and superharmonic imaging [14–17].

In contrast, the laser ultrasound transducer (LUT) is an alternative emerging technology due to its high power density, high frequency, broad bandwidth, and wireless device operation [18–27]. The LUT utilizes the photoacoustic (PA) effect that converts absorbed photon energy to acoustic waves. Since the LUT uses a short-pulse laser with high-density energy in a short duration (3-10 ns), the acoustic waves are usually characterized with high frequency (10⁰-10¹ MHz) and nanoseconds of pulse width [9,18,28,29].

As the LUT is promising for a broad range of applications, it is necessary to customize the LUT output characteristics or even break the current LUT limit to achieve the application-specific requirements. For example, broader -6 dB bandwidth is required for higher axial resolution imaging [14–17]; The medical lithotripsy and plaque disruption benefit from the higher positive pressure; higher negative pressure is desired in cavitation-related ultrasound therapies [30]; both high positive pressure and broad -6dB bandwidth are required for the high precision operation ablating malign tumors while avoiding the damage to the vital tissues [30]. In addition, low energy conversion efficiency (~1%) is another challenge in the LUT devices as compared with the traditional PZT transducers (~70%), which leads to excessive heat generation and limits the laser fluence [28].

Carbon-based nanomaterials and polydimethylsiloxane (PDMS) are commonly used for PA nanocomposite fabrication due to the extremely high light absorption of carbon and the excellent thermal expansion of PDMS [9]. To understand the effects of the material parameters on the LUT output, it is necessary to develop a method to predict the responses with higher accuracy and reliability. However, the relationship between the

composite material design parameters and the PA behaviors is not fully understood. Therefore, the design capability of the LUT devices is also limited due to the lack of knowledge predicting the multiphysics behavior of PA nanocomposites, including optical, thermal, mechanical, and acoustic responses. Previously, Huang et al. (2016) predicted the positive pressure output by a theoretical analysis within a 3 % error. However, the method showed the limitation to predict accurate waveform and negative pressure output [31]. More recently, Kwon et al. (2020) simulated the performance of carbon nanotube-coated polyethylene microspheres by the finite element analysis (FEA) method, but there was a significant discrepancy in the predicted positive pressure (1 MPa) with the experimental measurement $(2 \times 10^4 \text{ Pa})$ [32].

In this study, the FEA simulations for the PA nanocomposite behavior and the LUT device response, which are modeled in nanoscale and microscale, respectively, were used to predict the ultrasound generation. Firstly, the effective properties of the nanocomposites, such as the laser absorptivity, thermal expansion coefficient, Young's modulus, Poisson's ratio, and thermal conductivity, were estimated by the FEA using the unit cell model containing a single nanoparticle. Secondly, the LUT consisted of the laser window, nanocomposite and elastomer, was modeled for the FEA prediction of the PA wave generation. Lastly, the wave propagation and natural focusing in the water media were calculated by the theoretical equations. This integrated approach was validated by comparing the simulations with the experimental measurements. The relationship between the LUT output characteristics and the composite material parameters, including the particle size and volume fraction, was investigated by the computational parametric study.

2 Methods:

2.1 Prediction of effective properties of PA nanocomposites

The assumption that the composites' effective properties are the same as PDMS was one of the causes of the inaccuracy in the theoretical models in [31,33]. In this study, FEA simulation (COMSOL Multiphysics 5.5) is used to understand the relationship between the composite design parameters and the effective physical properties [34–40]. The composite design variables used in this study are the type and the size of the carbon-based nanomaterials. The physical properties such as Young's modulus *E*, Poisson's ratio

 ν , thermal expansion coefficient β , thermal conductivity K, and absorption coefficient α are derived from the FEA results. The model employed the unit cell model to reduce the computational burden (**Fig. 1**). The 0-dimensional (0-D) spherical particle (**Fig. 1a**) was used to represent the carbon black (CB) or the candle soot nanoparticle (CSNP), and the 1-dimensional (1-D) cylindrical particle (**Fig. 1b-e**) was for the carbon nanofiber (CNF). To implement the random orientation effect of the 1-D particles dispersed in the thin film on x-y plane, the particles oriented in (100), (110), (010), and (-110) directions in the xyz-coordinates were modeled to calculate the averages of the effective properties. The laser incidents along the z-axis in the simulations.

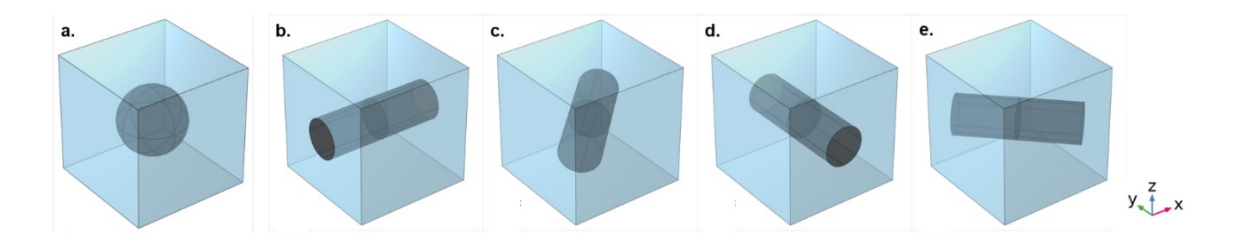


Fig. 1. FEA unit models for nanocomposites containing (a) spherical particle and (b)-(e) cylindrical fibers in (100), (110), (010), and (-110) directions.

For the mechanical properties, the volume average strains ε_x , ε_y , and ε_z are estimated in the FEA (Solid Mechanics modules) by applying axial force F in the z-direction (detailed information in Supplementary Information Section 2.1). The Young's modulus E and Poisson's ratio ν can be calculated by the equations:

$$E = \frac{F}{S\varepsilon_7} \tag{1}$$

$$\nu = -\frac{\varepsilon_x}{\varepsilon_z} = -\frac{\varepsilon_y}{\varepsilon_z} \tag{2}$$

where S is the cross-section area normal to F.

For the thermal conductivity K, Heat Transfer module was employed. The bottom and top surfaces were set to constant temperatures, and the surface average heat flux in the z-direction Φ_z was measured on the horizontal plane (x-y plane) when the temperature was stable (**Fig. S2c**). Periodical boundary conditions were used for the four vertical surfaces. The detailed boundary condition is shown in Supplementary Information Section 2.2. The thermal conductivity K can be calculated by the following equation:

$$K = \frac{\Phi_z d}{A^T} \tag{3}$$

where d is the thickness of the model (length in the z-direction), and ΔT is the difference of the temperatures applied on the top and bottom surfaces.

For the thermal expansion coefficient, COMSOL Heat Transfer and Solid Mechanics modules were coupled to simulate the mechanical strain response to the temperature change. The initial temperature was set to the ambient temperature (293 K). The top surface was set as the heat source with a constant temperature (600 K). Other detailed boundary conditions are shown in Supplementary Information Section 2.3. The stationary simulation was used to observe the responses at stable conditions. The thermal expansion in *i*-direction β_i can be calculated by the equation:

$$\beta_i = \varepsilon_i / \Delta T \ (i = x, y, z) \tag{4}$$

where ε_i is the volume average strain in *i*-direction estimated by the FEA, and ΔT is the difference of the temperatures before and after heating ($\Delta T = 307 \text{ K}$).

For the absorption coefficient, the incident light enters through the top surface, and the transmitted light was measured at the bottom (**Fig. S2**). The vertical boundaries were set as periodical conditions (detailed in Supplementary Information 2.4). The absorptance A and the reflectance R were estimated at 532 nm by COMSOL Wave Optics. The absorption coefficient α can be calculated by the equation:

$$\alpha = -\ln\left[(1 - \frac{A}{1 - R})/d\right] \tag{5}$$

Lastly, the composite's effective mass density ρ_e and heat capacity C_P were estimated by the theoretical equations:

$$\rho_e = f_{V1}\rho_1 + f_{V2}\rho_2 \tag{6}$$

$$C_P = \frac{c_{P1}f_{V1}\rho_1 + c_{P2}f_{V2}\rho_2}{f_{V1}\rho_1 + f_{V2}\rho_2} \tag{7}$$

where C_{Pi} , f_{Vi} , and ρ_i are the heat capacity, volume fraction, and density of the composite phases i (1: particle, 2: matrix), respectively.

2.2 FEA model for LUT device

The three-layered LUT structure in a water medium was built in COMSOL Multiphysics (Fig. 2). Four physics solvers, including Radiation in Absorbing-scattering Media (rasm), Heat Transfer in Solids (ht), Solid Mechanics (solid, not including water), and Pressure Acoustic (actd, only for water), were employed in the sequential energy conversions from light absorption to acoustic wave. Three Multiphysics couplings were

used to build the relation between different physics solvers: Heat Transfer with Radiation in Absorbing-Scattering Media built the Laser-thermal coupling between *rasm* and *ht*; Thermal Expansion built the thermo-mechanics coupling between *ht* and *solid*; and Acoustic-Structure Boundary built the mechanics-acoustic coupling between *solid* and *actd*.

The boundary conditions for each model block are shown in **Fig. 2**. The width (vertical length) of the model was set as 1 μ m. The thickness (horizontal length) of the substrate is 1 μ m to decrease the computation load by assisted of the fix boundary condition. The water media was set as 20 μ m with a perfect match layer at the end of the model to mimic a unlimited open media. The composite layer and protection layer thicknesses were adjustable depending on the specific experimental setup. The mesh type was the free triangular, and the mesh size was controlled under 1/5 incident laser wavelength (laser wavelength is 532 nm).

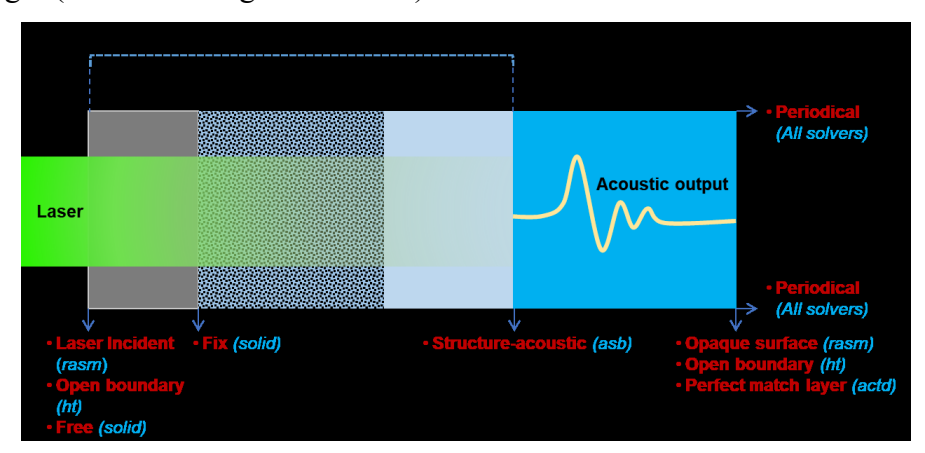


Fig. 2. Schematic of the LUT device structure in a water medium (not in scale). The model's boundary conditions (red bold) are shown for the corresponding solvers (blue italic) (i.e., rasm, ht, solid, asb, and actd).

2.3 Wave propagation in media:

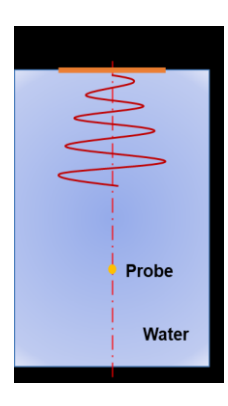


Fig 3. Wave propagation in the water medium.

The acoustic wave pressure detected at a distance from the LUT in the water (**Fig.** 3) can be analytically estimated as follows [41]:

$$p(\mathbf{r},t) = -\frac{jk}{2\pi}\rho c u_0 e^{-j\omega t} \int_{-\infty}^{\infty} \int_{-\infty}^{\infty} A(x_0, y_0) \frac{e^{j|r-r_0|}}{|r-r_0|} dx_0 dy_0$$
 (8)

$$u_0 = \frac{p_0}{\rho c} \tag{9}$$

$$A(x_0, y_0) = 1 (10)$$

where p(r,t) is the acoustic pressure at a location r at a time t, ρ is the density of propagation media (i.e., water), c is the sound speed in the media, p_0 is the acoustic pressure at the LUT surface (water-side of PDMS protection layer) derived from the FEA simulation, ω is the angular frequency of the acoustic wave at the LUT surface, k is the wavenumber, u_0 is the LUT surface velocity (thermal expansion velocity), and $A(x_0, y_0)$ is the LUT surface velocity distribution function. According to the Fresnel approximation for a relatively large wave source (aperture size $D \gg$ acoustic wavelength), Equation (8) can be simplified by:

$$\frac{e^{ik|r-r_0|}}{|r-r_0|} \approx \frac{e^{ikz}}{z} e^{ik[(x-x_0)^2 + (y-y_0)^2]/(2z)}$$
(11)

The aperture size D is equal to the effective diameter of the laser beam. The spatiotemporal theoretical acoustic pressure p(r,t) can be calculated by:

$$p(\mathbf{r},t) = -\frac{jk}{2\pi} p_0 e^{-j\omega t} \int_{-\infty}^{\infty} \int_{-\infty}^{\infty} \frac{e^{ikz}}{z} e^{ik[(x-x_0)^2 + (y-y_0)^2]/(2z)} dx_0 dy_0$$
 (12)

3 Results and Discussion:

3.1 Model validation

The hierarchical approach, including the effective property estimation, the LUT device simulation, and the wave propagation model, was validated by comparing the reproduced results with the experimental data in the literature, where the LUTs are composed of various carbon particles, such as carbon soot nanoparticle (CSNP), carbon nanofiber (CNF), and carbon black (CB), dispersed in PDMS [18]. Material and experimental conditions, including the particle volume fraction, particle size, and incident laser wavelength, were set identical with the literature [18]. Firstly, the composites' effective properties (Young's modulus E, Poisson's ratio ν , absorption coefficient α , thermal expansion coefficient β , and thermal conductivity K) were estimated by the unit cell FEA. The mechanical, optical, and thermal responses of the unit cells are shown in

Table S1-S4 in Supplementary Information. The estimated effective properties of composites are summarized in **Table 1** with the properties of the bare PDMS, a glass substrate, and water [31]. Secondly, the estimated properties were used in the PA layer of the LUT device simulation. The input laser fluence was 3.58 mJ/cm², and the thickness of each device layer was modeled based on the information shown in [18]. Detailed dimensional information of the device layers is shown in Supplementary Information **Table S5**. The FEA-based acoustic pressure profiles at the LUT surface in the time and frequency domains are shown in **Fig. 4 (a)-(c)** as compared with our previous theoretical analysis model (Huang's model) used in the literature [31].

Table 1. Material properties of the individual constituents and the estimated effective properties of carbon embedded PDMS composites (9 vol% CSNP, 1.77 vol% CNF and 47 vol% CB.)

	Glass	Water	PDMS	СВ	CNF	9% CSNP	1.77 % CNF	47% CB
β [1/K]	_	_	3.30×10 ⁻	2×10-	2×10-	3.02×10 ⁻⁴	3.16×10 ⁻⁴	1.65×10 ⁻
C_p [J/(kg×K)]	1000	4200	1460	675	675	1390	1446	1088
ρ [kg/m ³]	2200	1000	970	1630	1630	1029	981	1284
K $[W/(m\times K)]$	2	0.65	0.16	150	150	0.207	0.16	0.773
α [1/ μ m]	0	0	0	32	32	1.31	0.47	10
E [kPa]	72×10^{6}	_	750	10^{7}	5×10 ⁸	951	791	2148
υ	0.17	_	0.49	0.2	0.35	0.49	0.49	0.486

Lastly, the acoustic pressure detected at a distance from the LUT device surface (4.2 mm in [18]) was calculated by Equation (12) using the pressure profiles obtained with the FEA simulation and the Huang's model for comparison. The detected pressure profiles based on the experimental results [18], the TAC model [31], and the FEA simulation are compared in **Fig. 4 (d)-(f)**. The peak positive and negative pressure, peak frequency, -6 dB bandwidth, and energy efficiency obtained by the prediction model and the measurement are summarized in **Table 2**. The energy efficiency η was calculated by the equations:

$$\eta = \frac{E_a}{E_{optical}} \tag{13}$$

$$E_a = \frac{1}{\rho c} S_L \int_0^\infty p_0^2(t) \, dt \tag{14}$$

where E_a is the acoustic signal energy, $E_{optical}$ is the laser pulse energy, and S_L is the laser beam area.

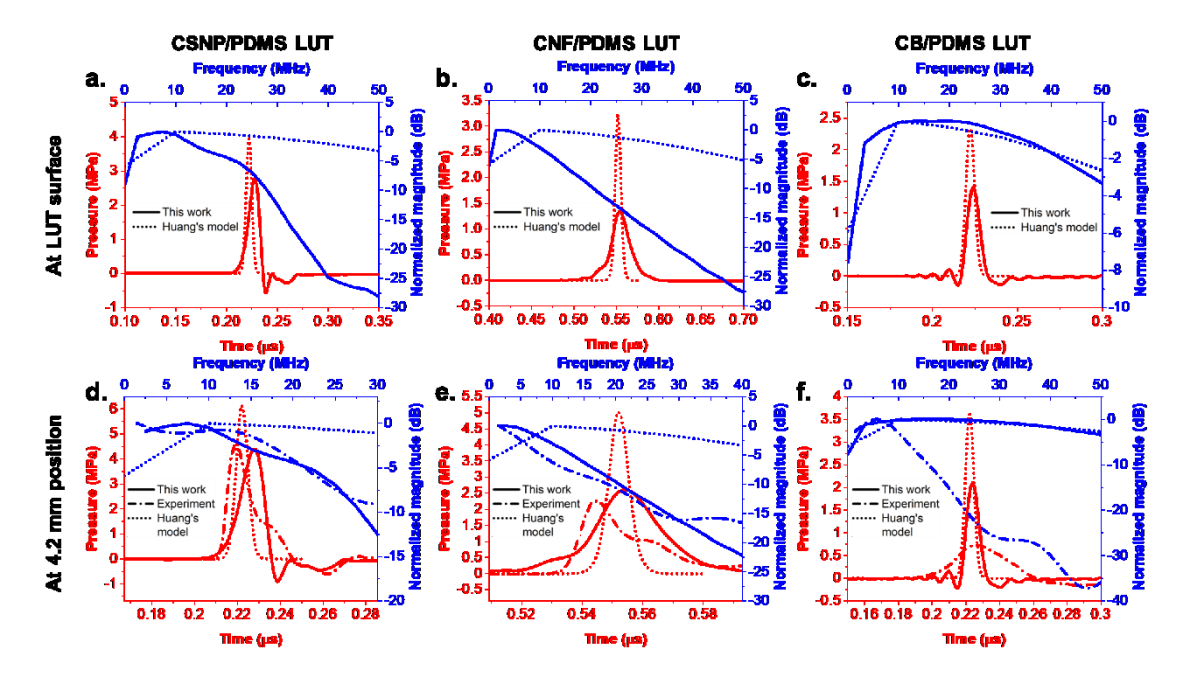


Fig. 4. The hierarchical predicting results for carbon-embedded PDMS LUT. (a)-(c) The acoustic waveform at LUT surface (water-side of the PDMS protection layer), This work vs. previous theoretical analysis model (Huang's model): (a) 9 vol% CSNP, (b) 1.77 vol% CNF, (c) 47 vol% CB. (d)-(f) The acoustic waveform at 4.2 mm from LUT surface, COMSOL/Propagation model (this work) *vs.* Huang's model/Propagation model vs. Experimental measurement shown in [18]: (d) 9 vol% CSNP, (e) 1.77 vol% CNF, (f) 47 vol% CB.

From Fig. 4 and Table 2, it can be known that the Huang's theory predicted results have significant differences on the acoustic output: the peak positive pressure is too high, the waveform is too sharp, negative pressure does not exist, and the bandwidth is extremely broad. Meanwhile, the hierarchical simulation approach has better performance than the theory. The simulation results of the 9 vol% CSNP/PDMS composite match well with the experimental data in both the time and frequency domain. The minor waveform difference at the time domain could be induced by the uncertainty in the experiment's measurement process. For the 1.77% CNF/PDMS composite, the simulated peak positive pressure and the -6 dB bandwidth simulation results (2.61 MPa and 13.6 MHz) are slightly higher than the measurement data (2.27 MPa and 7.2 MHz), the simulated peak frequency

(1.42 MHz) matches well with the measurement data (1.5MHz). The possible reason of broader predicted -6 dB bandwidth is that the high-frequency wave dissipated quickly in the unperfect CNF/PDMS composite structure of the experiment. On the other hand, the peak negative pressure in the simulation is smaller than the measurement as much as 0.23 MPa. The perfect fixed boundary condition in the simulation limited the LUT surface backward displacement, which attributes to the lower peak negative pressure. The experimental result of 47% CB/PDMS composite showed significantly reduced performance for all outcomes compared to the simulation. The deteriorated LUT performance is attributed to the particle agglomeration [18] and the reduced synthesis quality of the polymer matrix (PDMS) due to the too high particle concentration. Of note, the effective properties assigned to the LUT device layer are obtained by using the unit cell model, which assumes the individual particles are uniformly separated or not agglomerated. The results showed that the hierarchical simulation approach provides effective prediction in both time and frequency domains when the particle dispersion status in the composite is close to uniform.

Table 2. The hierarchical model estimation of Carbon/PDMS LUT acoustic output comparing with experiments and the Huang's model.

		Peak positive pressure [MPa]	Peak negative pressure [MPa]	Peak frequency [MHz]	-6 dB bandwidth [MHz]	Efficiency
9% CSNP	Experimental	4.66	0.6	10	22.5 (2.5-25, 225 %)	0.45%
	Huang's model	6.1	_	10	65 (0-65, 650%)	0.32%
	This work	4.4	0.89	7.49	21.3(1.5-22.8, 277%)	0.35%
1.77% CNF	Experimental	2.27	0.26	1.5	7.2 (1.5-9.7, 480%)	0.17%
	Huang's model	5	_	10	55 (0-55, 550%)	0.19%
	This work	2.61	0.03	1.42	13.6 (1.4-15, 957%)	0.23%
47% CB	Experimental	0.73	0.15	5.7	11.1 (1.5-12.6, 195 %)	0.03%
	Huang's model	3.62	_	10	75 (0-75, 750 %)	0.07%
	This work	2.12	0.84	13.28	56.8 (3.2-60, 428%)	0.05%

3.2 Composite layer optimization

Design parameters of photoacoustic nanocomposites, such as the particle size, shape, and volume fraction, are often arbitrarily chosen according to the designer's experience and insight, not by systematic procedures [18,28,42]. On the other hand, the approach in this study hierarchically combines the nanocomposite property estimation and the device output prediction providing a scientific design method to optimize the nanocomposites for the application-specific characteristics, such as the higher negative pressure or broader bandwidth. Herein, the design capability was demonstrated with the study models each composed of 1-D cylindrical and 0-D spherical nanoparticles mixed in PDMS. The parametric studies were conducted by sweeping the particle design parameters, including the volume fractions f_v (5, 9, 12, 15, 18, 21, 24, 27 and 30 vol%) and the particle diameters d (10, 15, 20, 30, 50, 80, 100, and 120 nm). For the composites containing the 1-D cylinder particles, the particle orientation changed from (100), (110), (010), and (-110) directions in the xyz-coordinates to simulate the directional distribution (Fig. S1 in the Supplementary Information). Then, the average of the directional properties was used in the subsequent LUT device simulation. The laser incidents along the z-axis and was linearly polarized in both x and y directions ($E_x = 1 \text{ V/m}$ and $E_y = 1$ V/m, respectively).

The effective properties of the CB/PDMS and CNF/PDMS composites are shown in **Fig. 5** and **Fig. 6**, respectively. For both cases, it was found that only the light absorption coefficient α is sensitive to the combination of the particle size and volume fraction. Other parameters, Young's modulus E, Poisson's ratio ν , thermal expansion coefficient β , and thermal conductivity K, are sensitive only to the volume fraction (**Fig. 5** and **Fig. 6**). The thermal conductivity K increases along with the particle size increases [43]. However, in this study, it is not sensitive to the particle size in the relatively narrow range (10 - 120 nm) compared to [43].

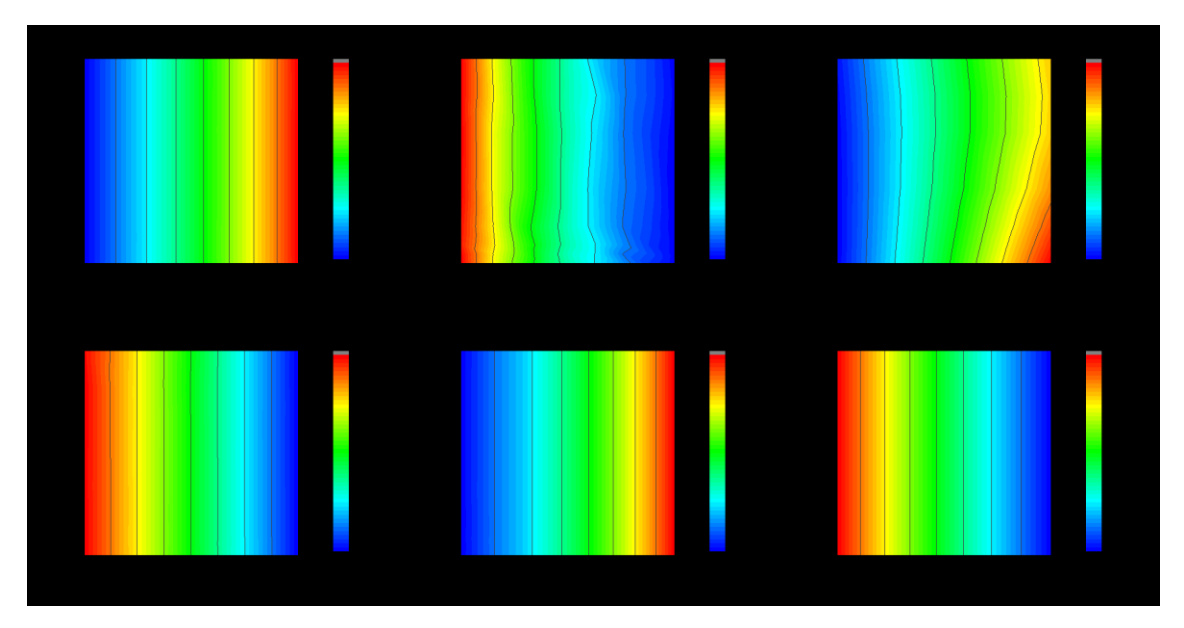


Fig. 5. CB/PDMS composite. Parametric study of the effective properties in terms of particle concentration and particle diameter. (a) Young's modulus E, (b) Poisson's ratio ν , (c) light absorption coefficient α , (d) thermal expansion coefficient β , (e) thermal conductivity K, (f) heat capacity C_p .

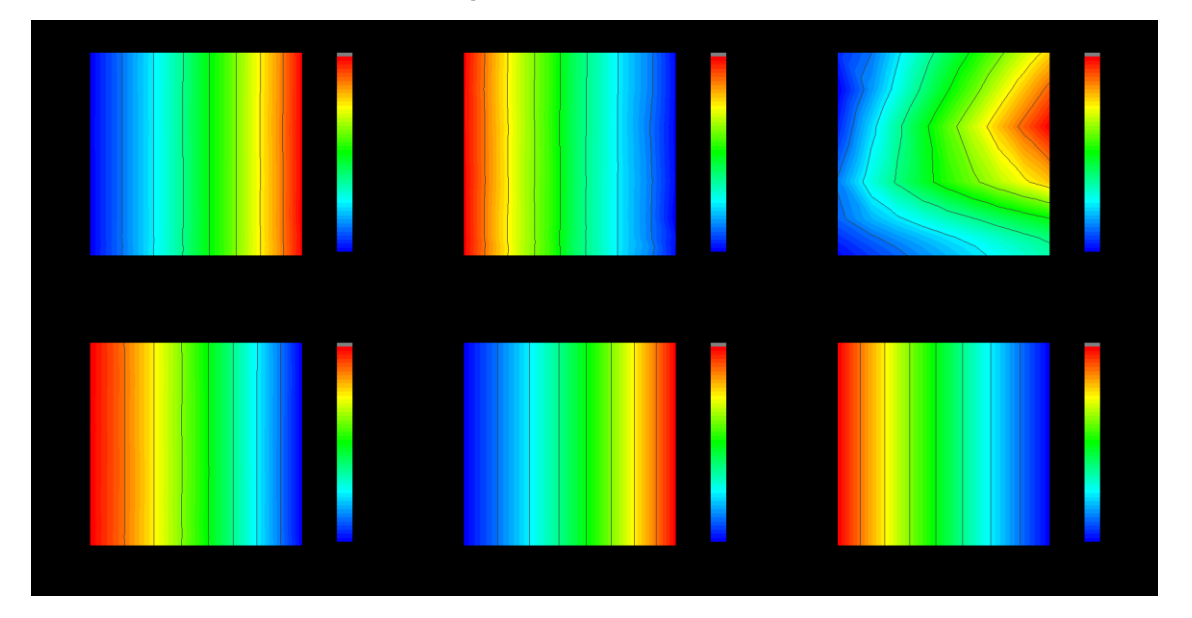


Fig. 6. CNF/PDMS composite. Parametric study of the effective properties in terms of particle concentration and particle diameter. (a) Young's modulus E, (b) Poisson's ratio ν , (c) light absorption coefficient α , (d) thermal expansion coefficient β , (e) thermal conductivity K, (f) heat capacity C_p .

Then, the FEA-derived effective properties of the nanocomposites were applied to the absorption layer in the LUT device simulations. The thicknesses of the absorption

layer and PDMS protection layer (**Fig. 1**) were set to be 2 μ m and 16 μ m, respectively, and the incident laser fluence was 3.58 mJ/cm². The photoacoustic pressure was monitored at the interface of the device and media (i.e., water). The pressure waveforms are shown in Supplementary Information **Fig. S3-S4**. The acoustic wave characteristics, including the peak positive pressure, peak negative pressure, peak frequency, -6dB bandwidth, and energy conversion efficiency, of the CB and CNF-based LUTs are shown in **Fig. 7** and **Fig. 8**, respectively.

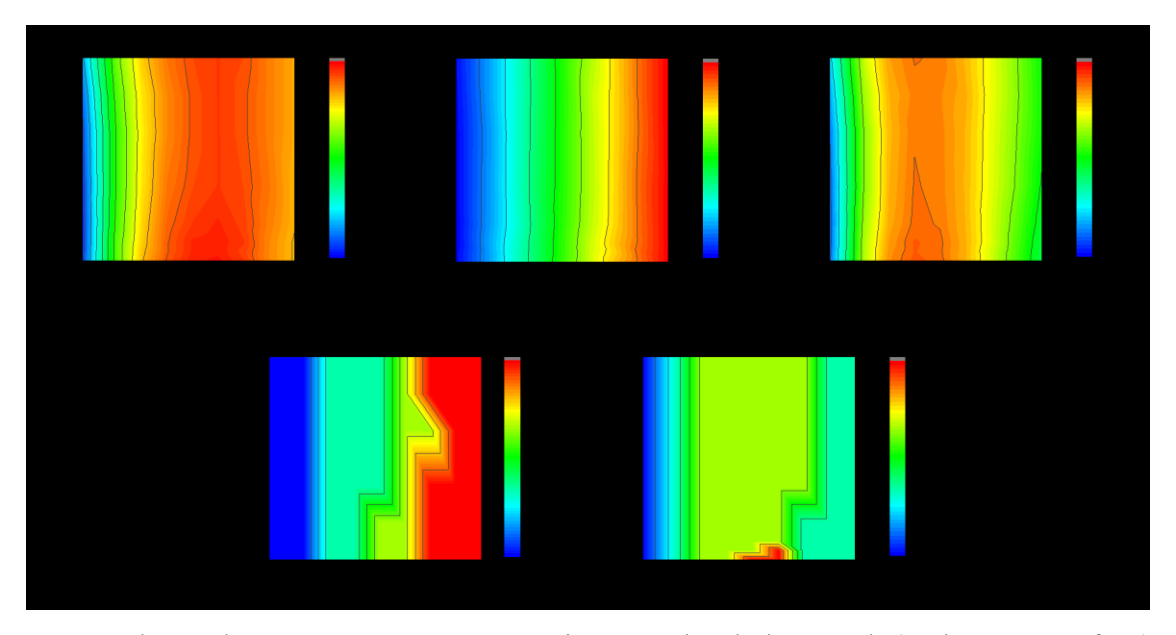


Fig. 7. The CB/PDMS LUT output acoustic wave simulation result (at the LUT surface). (a) peak positive pressure, (b) peak negative pressure, (c)energy conversion efficiency, (d) peak frequency, (e) -6dB bandwidth

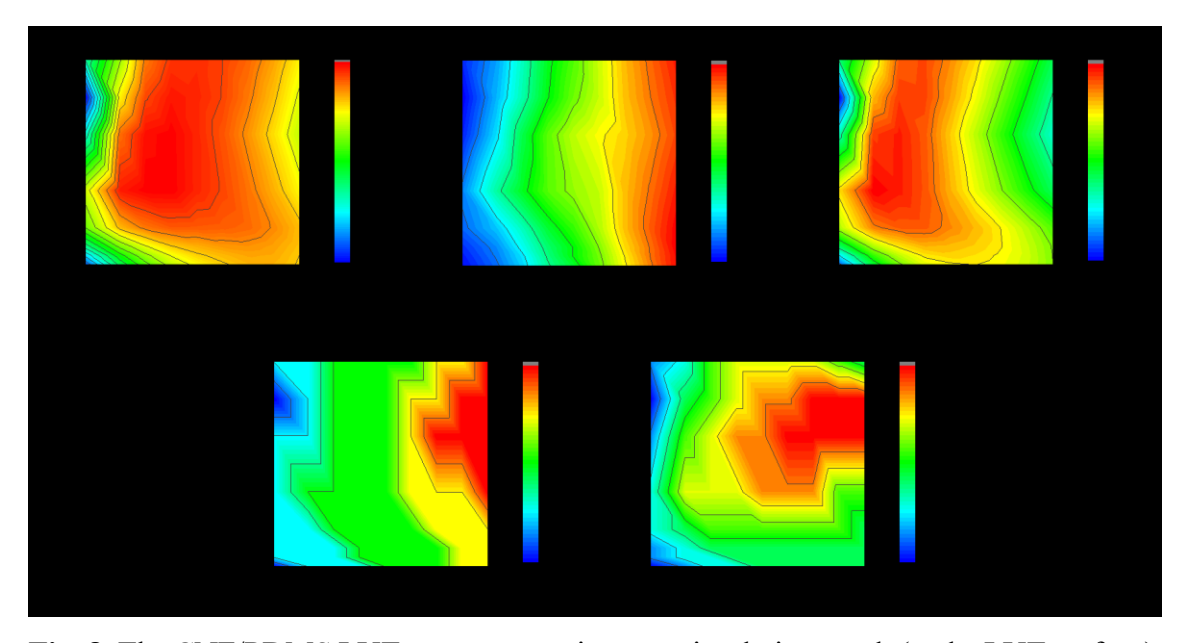


Fig. 8. The CNF/PDMS LUT output acoustic wave simulation result (at the LUT surface). (a) peak positive pressure, (b) peak negative pressure, (c) energy conversion efficiency, (d) peak frequency, (e) -6dB bandwidth.

For CB/PDMS-based LUT, the positive peak pressure has the maximum in the region of 10-40 nm particle diameter d and 20 % particle volume fraction f_v . The negative peak pressure and the positive peak frequency ascend with the increase of volume fraction. The broadest -6 dB bandwidth appears at d in the range of 10-20 nm and f_v in the range of 16-22%. The highest energy efficiency is located at d from 10-25 nm and f_v near 15%. In practical material design, for example, if a transducer needs higher positive pressure to obtain better performance in therapies such as lithotripsy and plaque disruption, the CB/PDMS transducer with d in the range of 10-40 nm and f_v near 20% will be recommended [30]. If both broader -6dB bandwidth and higher positive pressure are required for precisely ablating malign tumors, the intersection of their optimal regions, d around 10-20 nm and f_v near 20%, is the optimal scenario [30].

For CNF/PDMS LUT, the peak positive pressure had the maximum value at region d in the range of 40 - 80 nm and f_v in the range of 10 - 15%. The peak negative pressure ascends with the increase of volume fraction. The maximum peak frequency and broadest bandwidth appears at d in the range of 70 - 90 nm and f_v approximately in 25 - 30%. The highest efficiency is located at d in the range of 40 - 80 nm and f_v around 12%. If the broader -6dB bandwidth and higher peak positive pressure are required, the

intersection of their optimal regions, d around 70 - 80 nm and f_v near 20 %, is the optimal scenario.

4 Conclusion

In this study, a LUT hierarchical predicting approach was constructed. The effective properties estimation, LUT FEA model, and the propagating calculation in the media (water) were jointed to predicted the acoustic output of LUT. To validate the feasibility of our method, three different LUT, 9% CSNP/PDMS, 1.77% CNF/PDMS, and 47 % CB/PDMS, were used for the comparing simulation. For 9% CSNP/PDMS and 1.77% CNF/PDMS, the hierarchical predicting approach achieved excellent performance on both time and frequency domain output. Meanwhile, 47 % CB/PDMS result is not expectable due to the very high particle content.

Based on the hierarchical predicting approach, the parameter-sweep simulations were demonstrated to explore the optimal LUT design with variables as particle size (10 – 120 nm) and volume fraction (5 – 30 %). It was known from the composite effective properties prediction simulation that only light absorption coefficient was sensitive to both embedded particle size and volume fraction and other effective properties only response to the particle volume fraction. For different purposes, there were different optimal parameters for LUT design. For example, if one device need both high peak positive pressure for plaque disruption, a CB/PDMS transduce with particles with d in the range of 10-20 nm and f_v near 20% or a CNF/PDMS transduce with particles with d around 70-80 nm and f_v near 20% could be chosen as the design scenario.

Overall, this study provides one novel hierarchical FEA method to predict the acoustic output of the LUT accurately. This method has great potential for the LUT design and comparative research, including parameter optimization, new material direction, and surface-pattern design.

Acknowledgment

This article was supported in part by the U.S. Department of Energy (DOE) under Project No. DE-NE0008708. S.L. and J. R. were partially supported by the National Science Foundation under Grant No. 2031558 and the new faculty start-up fund at NCSU.

Declaration of interests

The authors declare that they have no known competing financial interests or personal relationships that could have appeared to influence the work reported in this paper.

Data availability

The raw/processed data required to reproduce the findings in the current manuscript cannot be shared at this time, as these data also form part of an ongoing study.

Reference

- [1] H.C. Klingler, M. Susani, R. Seip, J. Mauermann, N. Sanghvi, M.J. Marberger, A novel approach to energy ablative therapy of small renal tumours: laparoscopic high-intensity focused ultrasound, Eur. Urol. 53 (2008) 810–818.
- [2] J. Ninet, X. Roques, R. Seitelberger, C. Deville, J.L. Pomar, J. Robin, O. Jegaden, F. Wellens, E. Wolner, C. Vedrinne, Surgical ablation of atrial fibrillation with off-pump, epicardial, high-intensity focused ultrasound: results of a multicenter trial, J. Thorac. Cardiovasc. Surg. 130 (2005) 803-e1.
- [3] S.E.P. Burgess, R.H. Silverman, D.J. Coleman, M.E. Yablonski, F.L. Lizzi, J. Driller, A. Rosado, P.H. Dennis Jr, Treatment of glaucoma with high-intensity focused ultrasound, Ophthalmology. 93 (1986) 831–838.
- [4] C.M.C. Tempany, E.A. Stewart, N. McDannold, B.J. Quade, F.A. Jolesz, K. Hynynen, MR imaging—guided focused ultrasound surgery of uterine leiomyomas: a feasibility study, Radiology. 226 (2003) 897–905.
- [5] R. Muthaiah, J. Garg, Ultrahigh thermal conductivity in hexagonal BC6N- An efficient material for nanoscale thermal management- A first principles study, Comput. Mater. Sci. 200 (2021) 110773. https://doi.org/https://doi.org/10.1016/j.commatsci.2021.110773.
- [6] D. Shi, Y. Guo, Y. Qin, J. Song, Z. Liu, X. Chen, K. Luo, M. Bu, Y. Li, S. Du, The mechanical and thermal properties of (Th,U)Si compounds: A systematic density functional theory research, Comput. Mater. Sci. 188 (2021) 110148. https://doi.org/https://doi.org/10.1016/j.commatsci.2020.110148.
- [7] V.N. Thakur, S. Yadav, A. Kumar, Effect of bismuth substitution on piezoelectric coefficients and temperature and pressure-dependent dielectric and impedance

- properties of lead zirconate titanate ceramics, Mater. Today Commun. 26 (2021) 101846. https://doi.org/https://doi.org/10.1016/j.mtcomm.2020.101846.
- [8] Z. Wang, D. Hao, J. Wang, Y. Zhang, Study on the acoustic field characteristics of OPCM focusing transducer, Mater. Today Commun. 30 (2022) 103197. https://doi.org/https://doi.org/10.1016/j.mtcomm.2022.103197.
- [9] J. Kim, H. Kim, W.-Y. Chang, W. Huang, X. Jiang, P.A. Dayton, Candle-soot carbon nanoparticles in photoacoustics: advantages and challenges for laser ultrasound transmitters, IEEE Nanotechnol. Mag. 13 (2019) 13–28.
- [10] A.D. Maxwell, G. Owens, H.S. Gurm, K. Ives, D.D. Myers Jr, Z. Xu, Noninvasive treatment of deep venous thrombosis using pulsed ultrasound cavitation therapy (histotripsy) in a porcine model, J. Vasc. Interv. Radiol. 22 (2011) 369–377.
- [11] K.-W. Lin, Y. Kim, A.D. Maxwell, T.-Y. Wang, T.L. Hall, Z. Xu, J.B. Fowlkes, C.A. Cain, Histotripsy beyond the intrinsic cavitation threshold using very short ultrasound pulses: Microtripsy, IEEE Trans. Ultrason. Ferroelectr. Freq. Control. 61 (2014) 251–265.
- [12] X. Zhang, G.E. Owens, H.S. Gurm, Y. Ding, C.A. Cain, Z. Xu, Noninvasive thrombolysis using histotripsy beyond the intrinsic threshold (microtripsy), IEEE Trans. Ultrason. Ferroelectr. Freq. Control. 62 (2015) 1342–1355.
- [13] S. Liu, M.D. Islam, Z. Ku, A.M. Urbas, D.A. Boyd, W. Kim, J.S. Sanghera, J.E. Ryu, The polymer nanocomposites embedded particles size and agglomeration effect on the effective refractive index tuning, in: Nanoeng. Fabr. Prop. Opt. Thin Film. Devices XVIII, International Society for Optics and Photonics, 2021: p. 118020L.
- [14] T. Buma, M. Spisar, M. O'Donnell, A high-frequency, 2-D array element using thermoelastic expansion in PDMS, IEEE Trans. Ultrason. Ferroelectr. Freq. Control. 50 (2003) 1161–1176. https://doi.org/10.1109/TUFFC.2003.1235327.
- [15] T. Buma, M. Spisar, M. O'Donnell, Thermoelastic expansion vs. piezoelectricity for high-frequency, 2-D arrays, IEEE Trans. Ultrason. Ferroelectr. Freq. Control. 50 (2003) 1065–1068. https://doi.org/10.1109/TUFFC.2003.1226551.

- [16] E.J. Alles, S. Noimark, E. Zhang, P.C. Beard, A.E. Desjardins, Pencil beam all-optical ultrasound imaging, Biomed. Opt. Express. 7 (2016) 3704. https://doi.org/10.1364/boe.7.003696.
- [17] S. Noimark, R.J. Colchester, B.J. Blackburn, E.Z. Zhang, E.J. Alles, S. Ourselin, P.C. Beard, I. Papakonstantinou, I.P. Parkin, A.E. Desjardins, Carbon-Nanotube-PDMS Composite Coatings on Optical Fibers for All-Optical Ultrasound Imaging, Adv. Funct. Mater. 26 (2016) 8390–8396. https://doi.org/10.1002/adfm.201601337.
- [18] W.-Y. Chang, W. Huang, J. Kim, S. Li, X. Jiang, Candle soot nanoparticles-polydimethylsiloxane composites for laser ultrasound transducers, Appl. Phys. Lett. 107 (2015) 161903.
- [19] T. Buma, M. Spisar, M. O'donnell, High-frequency ultrasound array element using thermoelastic expansion in an elastomeric film, Appl. Phys. Lett. 79 (2001) 548–550.
- [20] R.J. Colchester, C.A. Mosse, D.S. Bhachu, J.C. Bear, C.J. Carmalt, I.P. Parkin, B.E. Treeby, I. Papakonstantinou, A.E. Desjardins, Laser-generated ultrasound with optical fibres using functionalised carbon nanotube composite coatings, Appl. Phys. Lett. 104 (2014) 173502.
- [21] H.W. Baac, J.G. Ok, A. Maxwell, K.-T. Lee, Y.-C. Chen, A.J. Hart, Z. Xu, E. Yoon, L.J. Guo, Carbon-nanotube optoacoustic lens for focused ultrasound generation and high-precision targeted therapy, Sci. Rep. 2 (2012) 989.
- [22] M. Faraz, M.A. Abbasi, P. Sang, D. Son, H.W. Baac, Stretchable and Robust Candle-Soot Nanoparticle-Polydimethylsiloxane Composite Films for Laser-Ultrasound Transmitters, Micromachines. 11 (2020) 631.
- [23] Q. Li, H. Zhu, C. Feng, Z. He, W. Dong, H. Yu, Simple yet universal fabrication strategy for a focused photoacoustic transmitter, Opt. Lett. 44 (2019) 1300–1303.
- [24] T. Lee, L.J. Guo, Highly efficient photoacoustic conversion by facilitated heat transfer in ultrathin metal film sandwiched by polymer layers, Adv. Opt. Mater. 5 (2017) 1600421.
- [25] Z. Chen, Y. Wu, Y. Yang, J. Li, B. Xie, X. Li, S. Lei, J. Ou-Yang, X. Yang, Q. Zhou, others, Multilayered carbon nanotube yarn based optoacoustic transducer

- with high energy conversion efficiency for ultrasound application, Nano Energy. 46 (2018) 314–321.
- [26] T. Yu, F. Jiang, Y. Chen, M. Cao, C. Wang, R. Qin, C. Guo, Acoustic properties of polyurethane composite with both millimeter-scale closed cavity and nanometer-scale semi closed cavity, Mater. Today Commun. 31 (2022) 103295. https://doi.org/https://doi.org/10.1016/j.mtcomm.2022.103295.
- [27] Q.-B. Nguyen, V.-H. Nguyen, C. Perrot, A.R. de Anda, E. Renard, S. Naili, Multiscale approach to characterize effective mechanical, hydraulic and acoustic properties of a new bio-based porous material, Mater. Today Commun. 26 (2021) 101938. https://doi.org/https://doi.org/10.1016/j.mtcomm.2020.101938.
- [28] W.-Y. Chang, X.A. Zhang, J. Kim, W. Huang, A. Bagal, C.-H. Chang, T. Fang, H.F. Wu, X. Jiang, Evaluation of photoacoustic transduction efficiency of candle soot nanocomposite transmitters, IEEE Trans. Nanotechnol. 17 (2018) 985–993.
- [29] J. Kim, W.-Y. Chang, H. Wu, X. Jiang, Optical fiber laser-generated-focused-ultrasound transducers for intravascular therapies, in: 2017 IEEE Int. Ultrason. Symp., IEEE, 2017: pp. 1–4.
- [30] J. Kim, W.-Y. Chang, B.D. Lindsey, P.A. Dayton, X. Dai, J.M. Stavas, X. Jiang, Laser-generated-focused ultrasound transducers for microbubble-mediated, dual-excitation sonothrombolysis, in: 2016 IEEE Int. Ultrason. Symp., IEEE, 2016: pp. 1–4.
- [31] W. Huang, W.-Y. Chang, J. Kim, S. Li, S. Huang, X. Jiang, A novel laser ultrasound transducer using candle soot carbon nanoparticles, IEEE Trans. Nanotechnol. 15 (2016) 395–401.
- [32] S.W. Kwon, W.Y. Choi, H.G. Jo, K.K. Park, Frequency modulation of laser ultrasound transducer using carbon nanotube-coated polyethylene microsphere, J. Acoust. Soc. Am. 147 (2020) EL351–EL356. https://doi.org/10.1121/10.0000952.
- [33] J. Li, Y. Yang, Z. Chen, S. Lei, M. Shen, T. Zhang, X. Lan, Y. Qin, J. Ou-Yang, X. Yang, Y. Chen, Z. Wang, B. Zhu, Self-healing: A new skill unlocked for ultrasound transducer, Nano Energy. 68 (2020) 104348.
 https://doi.org/10.1016/j.nanoen.2019.104348.

- [34] S. Liu, M.D. Islam, Z. Ku, D.A. Boyd, Y. Zhong, A.M. Urbas, E. Smith, J. Derov, V.Q. Nguyen, W. Kim, Novel computational design of high refractive index nanocomposites and effective refractive index tuning based on nanoparticle morphology effect, Compos. Part B Eng. (2021) 109128.
- [35] A.J. Berndt, J. Hwang, M.D. Islam, A. Sihn, A.M. Urbas, Z. Ku, S.J. Lee, D.A. Czaplewski, M. Dong, Q. Shao, Poly (sulfur-random-(1, 3-diisopropenylbenzene)) based mid-wavelength infrared polarizer: optical property experimental and theoretical analysis, Polymer (Guildf). 176 (2019) 118–126.
- [36] T. Bensattalah, M. Zidour, T.H. Daouadji, A new nonlocal beam model for free vibration analysis of chiral single-walled carbon nanotubes, Compos. Mater. Eng. 1 (2019) 21–31.
- [37] N. Bakhshi, F. Taheri-Behrooz, Length effect on the stress concentration factor of a perforated orthotropic composite plate under in-plane loading, Int. J. Compos. Mater. 1 (2019) 71–90.
- [38] R.R. Santhapuram, C. Phelan, M. Zou, A.K. Nair, The effect of dimensional parameters of multi-asperity surfaces on friction at the nanoscale, Comput. Mater. Sci. 191 (2021) 110276. https://doi.org/https://doi.org/10.1016/j.commatsci.2021.110276.
- [39] S. Liu, Fea Method Predicting the Refractive Index of Nano-Composite and Verified by Mwir Ormochalc Polymer Nano-Composite, (2020).
- [40] S. Liu, M.D. Islam, Z. Ku, A.M. Urbas, J. Derov, D.A. Boyd, W. Kim, J.S. Sanghera, J.E. Ryu, Novel Nanocomposite Refractive Index Tuning Mechanism Based on Controlling Embedded Particle Morphology, in: ASME Int. Mech. Eng. Congr. Expo., American Society of Mechanical Engineers, 2021: p. V003T03A011.
- [41] R.S.C. Cobbold, Foundations of biomedical ultrasound, Oxford university press, 2006.
- [42] B.Y. Hsieh, J. Kim, J. Zhu, S. Li, X. Zhang, X. Jiang, A laser ultrasound transducer using carbon nanofibers-polydimethylsiloxane composite thin film, Appl. Phys. Lett. 106 (2015). https://doi.org/10.1063/1.4905659.

[43] O. El-Kady, A. Fathy, Effect of SiC particle size on the physical and mechanical properties of extruded Al matrix nanocomposites, Mater. Des. 54 (2014) 348–353.